Proceedings of ASME Turbo Expo 2011
GT2011
June 6-10, 2011, Vancouver, British Columbia, Canada

GT2011-46253

THE ROLE OF TIP LEAKAGE VORTEX BREAKDOWN IN FLOW FIELDS AND AERODYNAMIC CHARACTERISTICS OF TRANSONIC CENTRIFUGAL COMPRESSOR IMPELLERS

Kazutoyo Yamada, Masato Furukawa, Hisataka Fukushima
Department of Mechanical Engineering
Kyushu University
744 Motooka, Nishi-ku, Fukuoka, 819-0395, Japan

Seiichi Ibaraki, Isao Tomita
Nagasaki Research & Development Center
Mitsubishi Heavy Industries, LTD.
5-71-1 Fukahhori-machi, Nagasaki, 851-0392, Japan

ABSTRACT

This paper describes the experimental and numerical investigations on unsteady three-dimensional flow fields in two types of transonic centrifugal compressor impellers with different aerodynamic characteristics. In the experimental results, the frequency spectra of the pressure fluctuations, which were measured with the high-response pressure transducers mounted on the casing wall just upstream of the impeller, turned out to be quite different between the compressor impellers at stall condition. The simulation results also showed different stall pattern for each compressor impeller. In the compressor impeller with a better performance at off-design condition, the stall cell was never formed despite decreasing flow rate and instead all the passages were covered with a reverse flow near the tip, where the vortex breakdown happened in the tip leakage vortex of full blade and led to the unsteadiness in the impeller. The vortex breakdown happened in all the passages prior to the stall and generated a blockage near the tip. This means that even with the advent of rotating stall the flow could not return to a normal undistorted condition in unstalled region, because all the passages are already occupied by the blockage due to the vortex breakdown. As a result, the rotating stall cell could not appear in the impeller. In the other compressor impeller, the rotating stall cell was formed at stall inception without the vortex breakdown in the tip leakage vortex of full blade, and developed with decreased flow rate.

NOMENCLATURE

C_m	: meridional velocity normalized by inlet tip speed
D	: dissipation term
H_{n}	: normalized helicity
k	: turbulent kinetic energy
l	: length scale
L	: chord length
M_r	: relative Mach number
P	: static pressure
P_0	: stagnation pressure at impeller inlet
P^*	: normalized pressure ($= P/q_t$)
P_s	: wall pressure coefficient ($= (P-P_0)/q_t$)
Q	: normal volume flow rate
q_t	: dynamic pressure based on inlet tip speed
t^*	: normalized time based on blade passing period
x	: chordwise distance from leading edge
δ	: boundary layer thickness
δ^*	: displacement thickness
Δ	: grid spacing
ξ_n	: absolute vorticity magnitude
ρ	: density
ω	: angular velocity of impeller

INTRODUCTION

The pressure ratio of centrifugal compressor in turbochargers tends to be higher according to demands of downsizing of engines and increasing their specific output power. It follows that the inlet Mach number, which is one of the most influential parameter to the performance of centrifugal compressors, is becoming more than 1.0, even in smaller-size centrifugal compressors as in automotive turbochargers. The efficiency becomes lower with increasing Mach number, and reduces further in the transonic centrifugal compressors due to the occurrence of shock wave. The shock wave formed at the inducer interacts with the blade surface boundary layer and the tip leakage vortex, which results in the generation of additional losses [1, 2].

The centrifugal compressors like in turbochargers have to operate from near surge limit to choke limit and requires a wide operating range. However, contrary to the increase in the pressure ratio, the operating range becomes narrower. The compressors may operate under the rotating stall at off-design condition near surge. The rotating stall is the main cause for the deterioration of compressor performance, and leads to excitation of mechanical vibrations as well, which sometimes limit the operating range [3]. Therefore, the expansion of the operating range and higher performance at off-design condition are important issues for the compressors.

In axial compressors, it is known that the tip clearance flow, which generates the tip leakage vortex, has a great influence on the aerodynamic performance as well as the compressor stability. Recent works suggest that the breakdown of the tip leakage vortex happens at near-stall condition and may be related to the compressor instability [4–8]. As for centrifugal compressors, a number of works has contributed to a basic understanding of the flow field such as secondary flow patterns and vortical flow structures [9–11]. Senoo and Ishida studied the effect of tip clearance on the compressor performance and developed the theory on the tip clearance loss of centrifugal impellers [12]. Unfortunately, however, there are few investigations on the association between the tip clearance flow and compressor stability [3, 13, 14].

The purpose of this study is to clarify the influence of the tip leakage vortex on the aerodynamic performance and compressor stability. Two types of transonic centrifugal compressors with different aerodynamic characteristics were analyzed using the time-accurate DES (Detached-Eddy Simulation) to investigate the difference in the tip leakage flow fields at off-design condition. In the experiment, pressure fluctuations on the casing wall were measured by the high-response pressure sensors to examine the unsteady characteristics of the tip leakage flow fields.

EXPERIMENTAL SETUP

Test Compressors

Two types of transonic centrifugal compressor, which are compact size centrifugal compressors with splitter blades for automotive turbochargers, were studied. The specification of the test compressors is given in Table 1. Both compressors have an open-type backswept impeller that is coupled with vaneless diffuser and scroll. A blade count of the impeller is different between two compressors. One impeller has 10 blades in total with 5 splitter blades (hereafter referred to as C_A), and the other has 8 blades in total with 4 splitter blades (hereafter referred to as C_B). The tip clearance is the same size of 0.3 mm in each impeller. All the other dimensions are nearly same among the compressors. At the design condition, the rotation speed of the impeller is 160,000 rpm, and the normal volume flow rate Q is 0.130 m^3/s for the compressor C_A and 0.117 m^3/s for the compressor C_B. As for the total pressure ratio, which is defined at the impeller upstream and the scroll exit, the compressor has very close performance each other. The tip speed is nearly equal to the speed of sound in each impeller, that is, the inlet flow exceeds the Mach number of 1 near the tip.

Table 1. Specification of the test compressors

	C_A	C_B
Number of Full Blade	5	4
Number of Splitter Blade	5	4
Impeller Inlet Diameter [mm]	39.5	37.1
Impeller Exit Diameter [mm]	50.0	49.6
Diffuser Exit Diameter [mm]	71.5	71.5
Diffuser Exit Width [mm]	3.6	3.2
Tip Clearance [mm]	0.3	0.3
Drive Shaft Speed [rpm]	160,000	160,000
Flow Rate [m^3/s]	0.130	0.117
Total Pressure Ratio	2.06	2.05

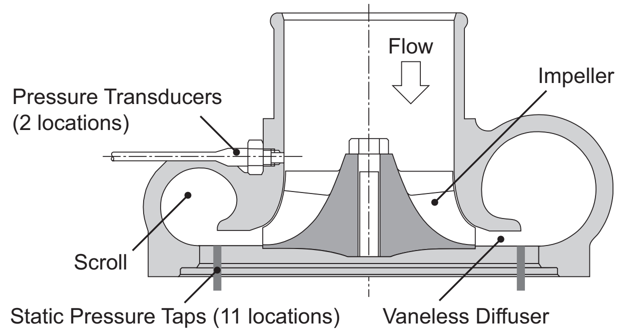

Figure 1. Cross section of compressor C_A

Measurement Method

The meridional cross section of the compressor C_A is shown in Figure 1. In this facility, the ambient air is sucked into the compressor. The total pressure and the total temperature were obtained at the impeller inlet and the scroll exit, and the mass flow rate was also measured downstream of the compressor. At the diffuser exit, static pressures on the hub were acquired by pressure taps mounted on 11 circumferential locations, and the total pressure was estimated from these hub static pressures and the scroll exit measurement data of the total pressure, the total temperature, and the mass flow rate. The unsteady characteristics were examined by a simultaneous pressure measurement with two high-response pressure transducers (Entran EPH-L1), which were mounted on the casing wall 3.0 mm upstream of the impeller leading edge at a circumferential interval of 30 degrees.

NUMERICAL METHOD

Flow Solver

The simulations in the present study were carried out using an in-house CFD code that had been developed and validated by the authors [7, 8]. The code solves the three-dimensional compressible Navier-Stokes equations by using a fully-implicit scheme with a cell-centered finite volume method, and includes RANS, LES and DES methods for the turbulence modeling. The code is parallelized using MPI (Message Passing Interface) by introducing the multi-block grid system. The supercomputer FUJITSU PRIMEQUEST 580 in Kyushu University was used for the present calculations. One simulation case required about 350 hours of the CPU time.

The numerical method of the present code is outlined in the following. The inviscid flux is evaluated by the TVD scheme based on the approximate Riemann solvers, which is extended up to third-order accuracy by the MUSCL interpolation. The point Gauss-Seidel relaxation method is used for the time integration. To obtain a time-accurate solution, the second-order backward difference is applied to the temporal derivative and the inner iteration is conducted at each time step. In this study, we set the inner iteration to 4 times. A time step size was set small enough to include at least 1,300 time steps in the blade passing period.

The DES in the present study is formulated based on the low Reynolds number k-ω turbulence model [15]. The dissipation term in the k-equation of the k-ω turbulence model is modified as follows [16]:

$$D^k_{\mathrm{DES}} = \rho k^{3/2}/\tilde{l} \tag{1}$$

$$\tilde{l} = \min(l_{k-\omega}, C_{\mathrm{DES}}\Delta) \tag{2}$$

where l is the turbulent length scale, Δ is the local grid spacing, and C_{DES} is a calibration constant of the DES formulation, which was set to 1.60 in this study. Equation (2) plays a role in switching the turbulence analysis method between RANS and LES according to the turbulent length scale. The model reduces to the k-ω turbulence model for RANS calculation if $l_{k-\omega}$ is selected and the sub-grid scale model for LES if $C_{\mathrm{DES}}\Delta$ is selected. Since the length scale becomes small near the wall, the switch from RANS to LES can take place somewhere inside the boundary layer, and then the main flow region including free shear flows is calculated by the LES-like formulation.

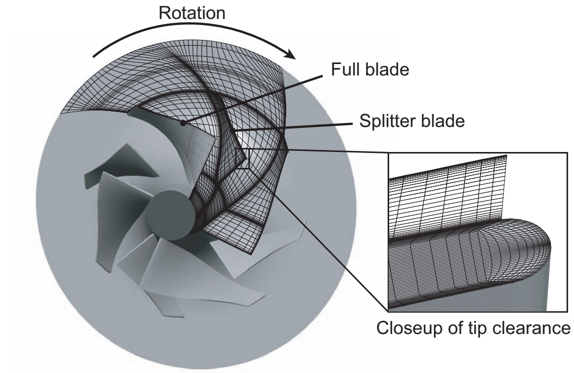

Figure 2. Computational grid of the compressor C_B (every 3 lines)

Computational Grid

Figure 2 shows the computational grid used in the compressor C_B simulation. In the figure, the grid is shown for only one passage of the full blade. The computational domain consists of the inlet block upstream of the impeller, which is omitted from the figure for viewability, the impeller block, and the vaneless diffuser block. The structured H-type grid was generated in each block by using the commercial mesh generation software Gridgen V15 (Pointwise, Inc.). The grid has 260 cells in the streamwise direction, of which 154 cells are included in the full-blade passage region and 94 cells are distributed along the splitter blade. Concerning the pitchwise direction, 80 cells are set in the blade-to-blade, that is 160 cells are included in the full-blade passage. In the spanwise direction, the grid contains 82 cells from the hub to the casing, of which 27 cells are in the tip clearance region. The grid has 14,966,288 in total (3,741,572 cells per passage). As for the grid used in the compressor C_A simulation, the number of cells in the pitchwise direction was changed to 64 cells according to the solidity increased. The spanwise cell number was also modified to be 75 cells from the hub to the casing and 24 cells in the tip clearance region. As a result, this grid amounts to 12,954,240 cells. The minimum spacing on the walls was set small enough to satisfy with the condition of $y^+ < 1$, so as to evaluate the viscous fluxes at the walls by applying the no-slip and adiabatic conditions without wall function method.

Boundary Conditions

In the flow solver, fictitious cells are introduced just outside all the boundaries of computational domain, in which the conserved variables are given so as to meet the boundary condition. The inflow boundary is set at the distance of 1.2 times the impeller inlet diameter apart upstream from the full blade leading-edge, for which the conserved variables in the fictitious cells are calculated so that total pressure, total temperature, tangential and radial flow angle (no pre-swirl) are specified. At the outflow boundary, which is located at the diffuser exit, all the conserved variables are extrapolated from the interior to the fictitious cells and the magnitude of the velocity in the cells is scaled so as to maintain the imposed total mass flow rate. In the DES calculation, we have also used the pressure distribution measured at the diffuser exit, in which the effect of scroll tongue is implicitly included, as the outlet boundary condition. It was confirmed that the similar results were obtained for both boundary condition. At the fictitious cells next to solid wall boundaries, the variables are given so that no-slip and adiabatic conditions can be satisfied.

RESULTS AND DISCUSSIONS

Performance Characteristics

Figure 3 shows the performance characteristics of total pressure ratio. The experiment shows that the compressor C_A achieves higher performance at high flow rates compared to the compressor C_B. However, it turns under the flow rate of approximately Q = 0.084 m^3/s. The total pressure ratio of the compressor C_A takes a local peak around Q = 0.102 m^3/s, which is considered to be the stall inception point. As will be shown later, disturbances actually start to appear at this operating point. In the case of the compressor C_B, the disturbances arise around Q = 0.084 m^3/s, where a slope of the characteristics slightly varies. These flow rates are hereinafter referred to as a ”disturbance onset point” for respective compressors. In the following, we will discuss about the flow fields at these disturbance onset points and their preceding operating points (Q = 0.111 m^3/s for compressor $C_A$and Q = 0.097 m^3/s for compressor C_B, which are hereinafter referred to as near disturbance onset point).

The figure includes the RANS results [17], which are from the steady-state single passage calculation. The RANS simulation mis-predicted the performance of the compressor C_A at lower flow rates than the stall inception point of Q = 0.102 m^3/s. On the other hand, in case of the compressor C_B, the RANS results are in good agreement with the experiment all over the range. The DES results from the full annulus calculations are coincident with the experimental ones for both compressors. The discrepancy between the RANS and DES results in the compressor C_A implies that the flow field is no longer axisymmetric due to the occurrence of the rotating stall and the periodicity assumption in the single passage RANS simulation is invalid. According to this interpretation, it follows that in the compressor C_B the flow field seems still axisymmetric even in lower flow rates.

Casing Wall Pressure Trace

Figure 4 shows the casing wall pressure traces measured at the upstream of the impeller for the compressor C_A. The results are raw data without low-pass filtering. The pressure is normalized by the dynamic pressure based on the tip speed of the impeller leading edge. Since the pressure transducers locate in the vicinity of the impeller leading edge, the pressure traces include the pressure fluctuation due to the blade passing, which is seen as a sawtooth waveform. At Q = 0.111 m^3/s, both of the experiment and simulation results show regular sawtooth waveforms. However, the sawtooth waveforms start to lose their cyclic patterns at Q = 0.102 m^3/s (shown by the circle in the figure). Therefore, this operating point is defined as the disturbance onset point for the compressor C_A.

Figure 5 shows the casing wall pressure traces for the compressor C_B. At Q = 0.097 m^3/s, unlike the compressor C_A, high

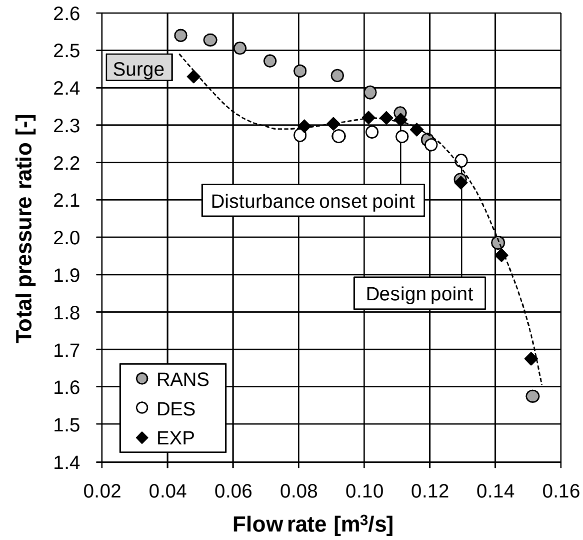

(a) compressor C_A

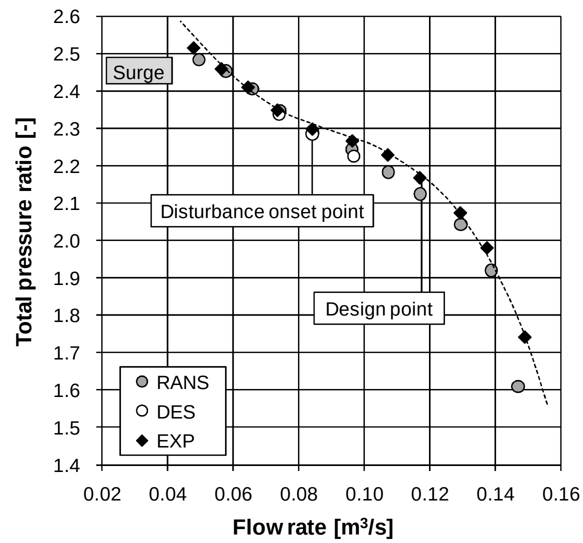

(b) compressor C_B

Figure 3. Performance characteristics of test compressors

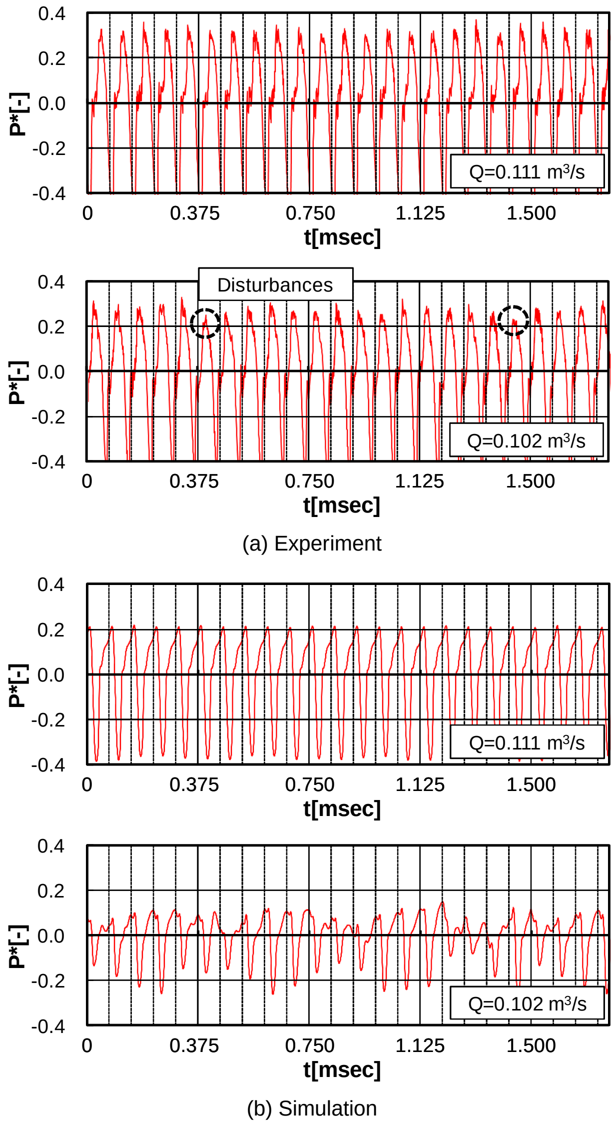

Figure 4. Pressure trace on the casing wall ahead of the impeller (compressor C_A)

frequency waves are superimposed on each sawtooth waveform, although the pressure fluctuation due to the blade passing is still identified. The experimental result shows that the high frequency waves have already appeared at the higher operating point (Q = 0.107 m^3/s). At Q = 0.084 m^3/s, the pressure traces are disturbed as much as it is hard to distinguish the pressure fluctuation due to the blade passing from the other waves. Therefore, this operating point, at which the periodic pressure fluctuation due to the blade passing cannot be identified, is defined as the disturbance onset point for the compressor C_B.

The characteristics of the disturbances have been analyzed by using the two pressure transducers located 30 degrees apart. In the compressor C_A, it turned out that the number of disturbance was one and its propagation speed was about 90% of the rotation speed. The simulation showed the same propagation speed and number of disturbance (refer to details in [14]). In the compressor C_B, however, they have been unclear, because the disturbance appeared as a transient and unstable phenomenon.

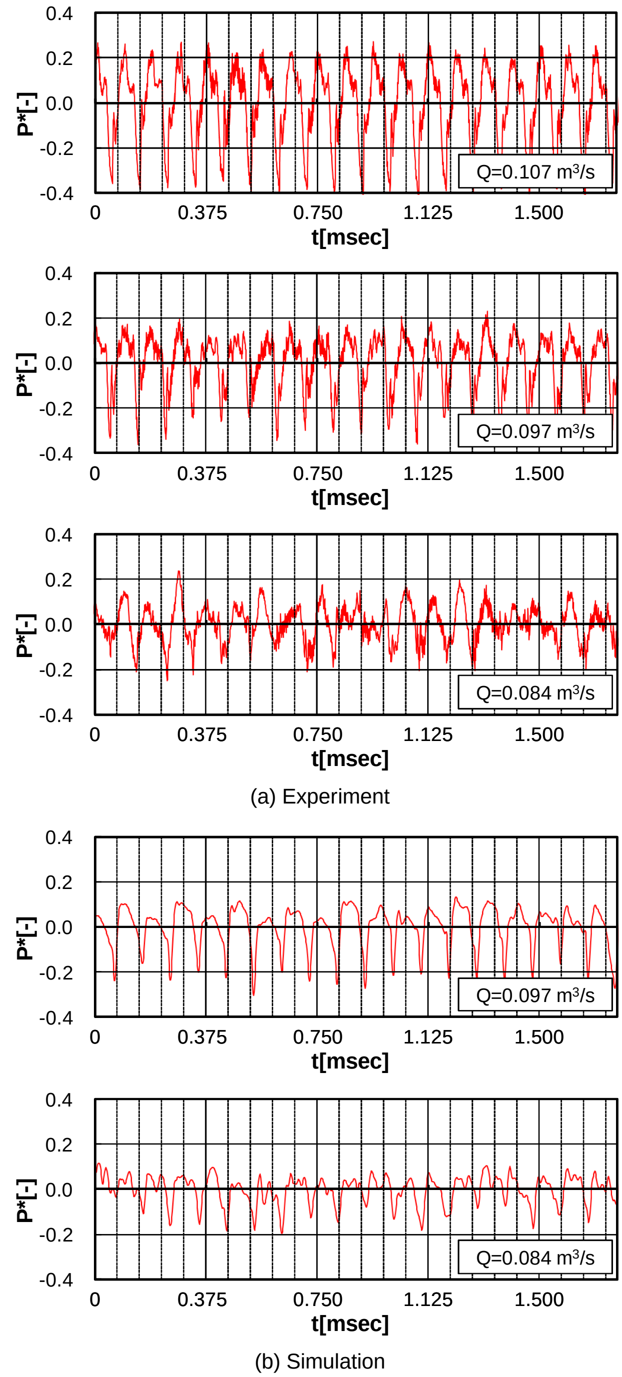

Figure 5. Pressure trace on the casing wall ahead of the impeller (compressor C_B)

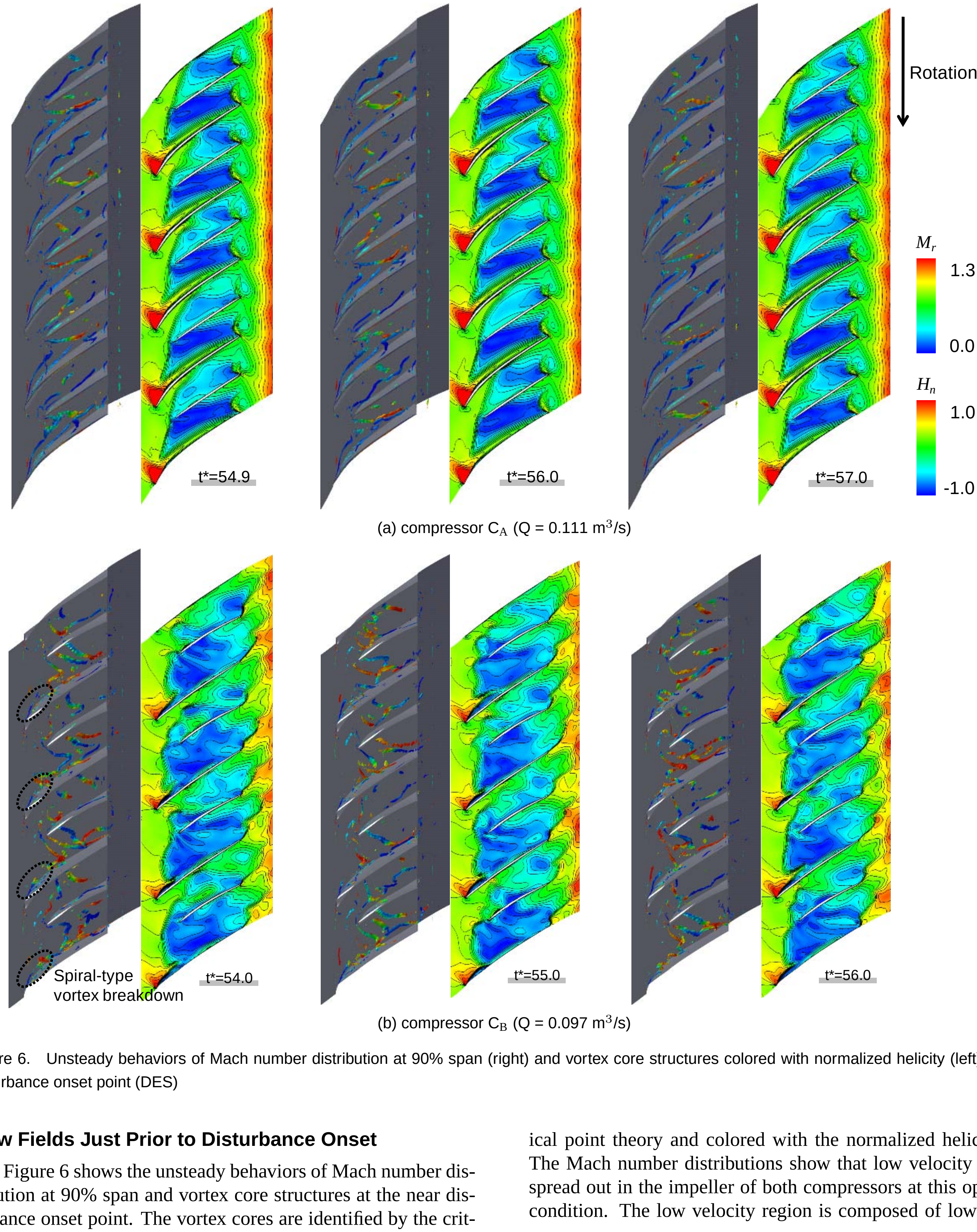

Figure 6. Unsteady behaviors of Mach number distribution at 90% span (right) and vortex core structures colored with normalized helicity (left) at near disturbance onset point (DES)

Flow Fields Just Prior to Disturbance Onset

Figure 6 shows the unsteady behaviors of Mach number distribution at 90% span and vortex core structures at the near disturbance onset point. The vortex cores are identified by the critical point theory and colored with the normalized helicity [7]. The Mach number distributions show that low velocity regions spread out in the impeller of both compressors at this operating condition. The low velocity region is composed of low energy fluids of the tip clearance flow. The low energy fluids are accumulating especially in the passage between the full blade suction surface and the splitter blade pressure surface. Comparing the low velocity region between the compressor C_A and C_B, the low velocity region in the compressor C_B is fluctuating with time. As mentioned below, in the compressor C_B the vortex breakdown has happened in the tip leakage vortex of full blade in every passage. The fluctuation of the low velocity region results from the unsteady behavior of the tip leakage vortex due to the spiral-type vortex breakdown. Although this fluctuation is still limited in the impeller, it has an influence on the pressure field even at the upstream of the impeller. As a result, the high frequency wave has appeared in the casing wall pressure trace for the compressor C_B, as shown in Figure 5. On the other hand, in the compressor C_A the vortex breakdown has not occurred in the tip leakage vortex of full blade at this operating condition. In fact, the Mach number distribution shows almost no fluctuation in the low velocity region.

Vortex breakdown Figure 7 shows vortex core structures of the time-averaged flow field at the near disturbance onset point. The vortex cores are colored with the normalized helicity. In the compressor C_B, the sign of normalized helicity on the tip

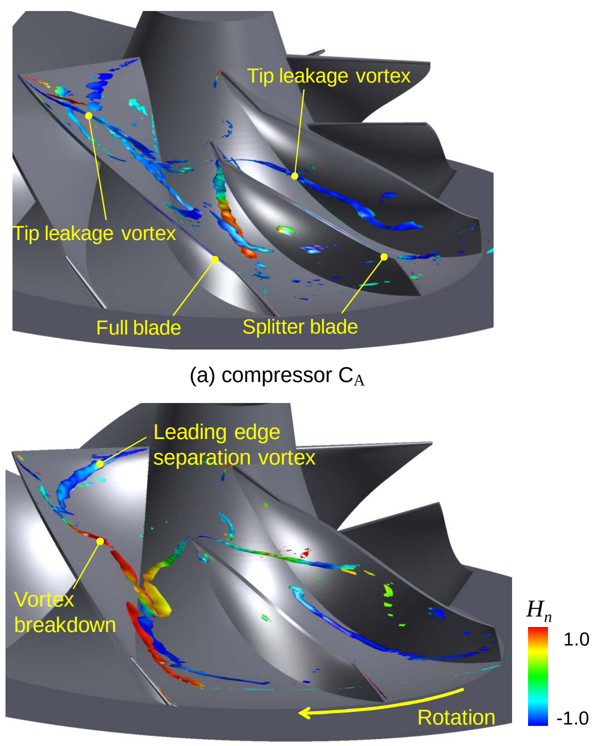

(a) compressor C_A

(b) compressor C_B

Figure 7. Vortex core structures of time-averaged flow fields at the near disturbance onset point (DES)

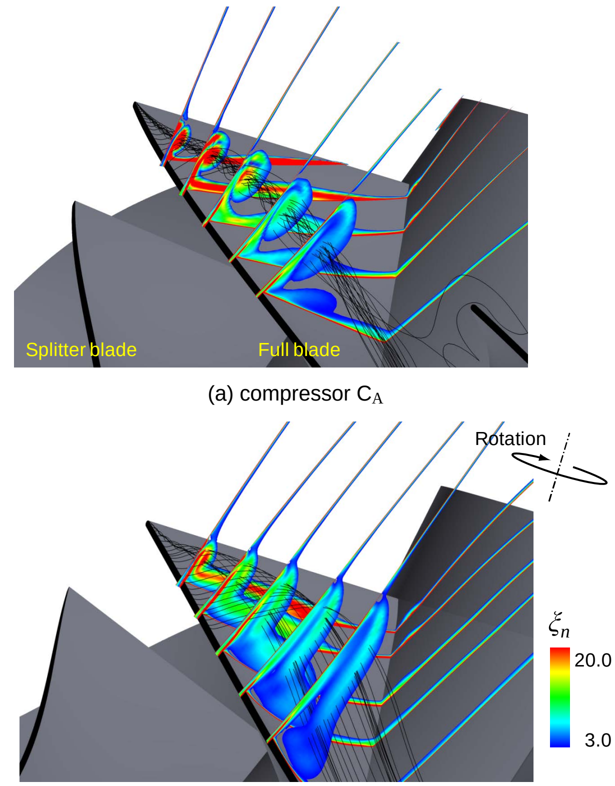

(a) compressor C_A

(b) compressor C_B

Figure 8. Time-averaged absolute vorticity distributions on crossflow plane at the near disturbance onset point (DES)

leakage vortex of full blade has inverted halfway. The sign of normalized helicity indicates the streamwise direction relative to the swirl direction of vortex, thus its change means appearance of reversed flow inside a vortex core. The normalized helicity in Figure 7(b) shows that a reversed flow is arising in the tip leakage vortex core of full blade in the compressor C_B. In other words, the tip leakage vortex of full blade has broken down in the compressor C_B. The change in the normalized helicity is found only in the compressor C_B, namely the vortex breakdown happens only in the compressor C_B. Time-averaged distributions of absolute vorticity magnitude are shown on several crossflow planes nearly perpendicular to the full blade tip leakage vortex in Figure 8. The tip leakage streamlines are also shown in this figure. The absolute vorticity magnitude ξ_n is normalized as follows:

$$\xi_n = \frac{\left|\vec{\xi}\right|}{2\omega} \tag{3}$$

where ω is the magnitude of the impeller angular velocity. As shown in the figure, the tip leakage streamlines are tightly rolling-up in the compressor C_A, while they are loosely rolling

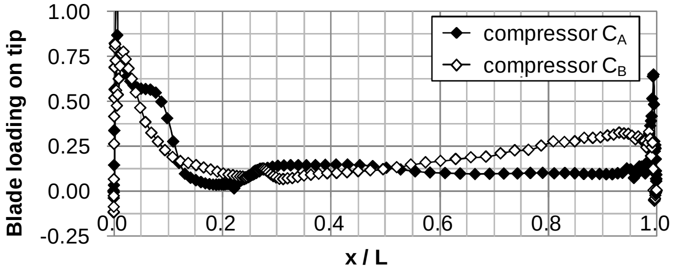

Figure 9. Time-averaged blade loading distributions at the full blade tip (DES)

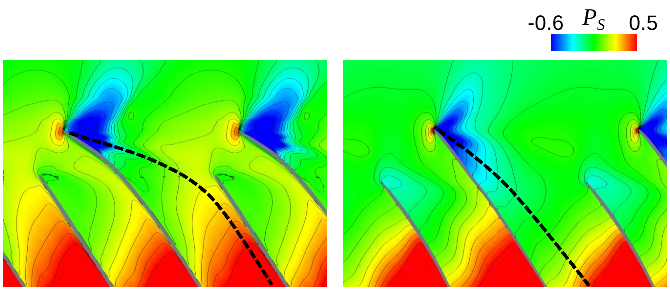

(a) compressor C_A (b) compressor C_B

Figure 10. Time-averaged pressure distributions on the casing wall (dash line: trajectory of tip leakage votex) (DES)

and expanding in the compressor C_B. The concentration of absolute vorticity is seen at around the center of the tip leakage vortex in the compressor C_A. In the compressor C_B, the absolute vorticity at the center of the tip leakage vortex has been lost and high absolute vorticity region has expanded. These phenomena seen in the compressor C_B indicate the vortex breakdown of the tip leakage vortex of full blade. The criterion for the vortex breakdown occurrence has not been revealed yet. However, it is known that the vortex breakdown occurs in a tightly rolling-up streamwise vortex under a strong adverse pressure gradient.

Figure 9 shows chordwise blade loading distributions at the full blade tip. The blade loading is defined by the pressure difference between the pressure and suction surfaces of full blade, and normalized by the dynamic pressure based on the blade tip speed. The abscissa is a chordwise distance from the leading edge, which is normalized by the chord length. The blade loading just near the leading edge, where the tip leakage vortex is rolling up, is almost the same level in both compressors. This means that the strength of the tip leakage vortex is also same between the two compressors. Figure 10 shows time-averaged pressure distributions on the casing wall at the near disturbance onset point. The dash lines in the figure indicate the trajectory of the tip leakage vortex of the full blade. In the compressor C_A, the tip leakage vortex of full blade interacts with the pressure surface of splitter blade at the leading edge, which is attributed to higher inlet angle and higher solidity of this impeller. The pressure distributions along the trajectory of the tip leakage vortex shown in

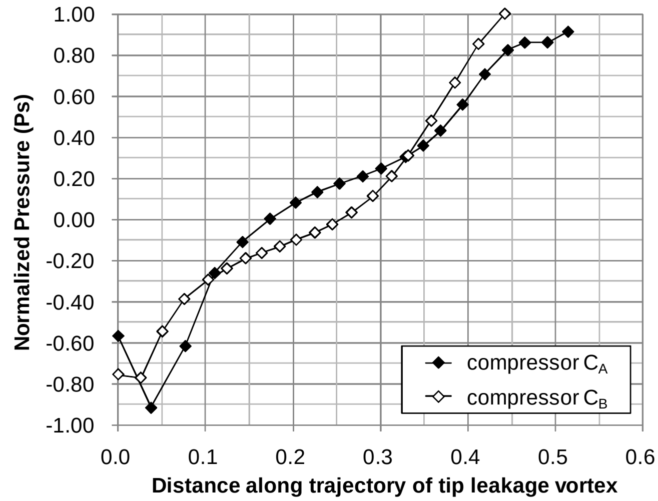

Figure 11. Pressure distributions along the trajectory of tip leakage vortex shown in Figure 10 (DES)

Figure 10 is presented in Figure 11. In the compressor C_A, there is a strong adverse pressure gradient in the normalized distance of 0.05 to 0.15. This is due to a relatively strong shock wave, and the tip leakage vortex is interacting with the shock wave, as shown in Figure 10. In spite of the strong adverse pressure gradient resulting from the shock wave, the vortex breakdown has never happened, because along with the main flow of high Mach number the tip leakage vortex core has had a high velocity. On the other hand, in the compressor C_B, a strong adverse pressure gradient appears in the aft-part of impeller passage. As shown in Figure 9, the blade loading of the compressor C_B impeller has aft-loaded profile. In the aft-part of impeller passage, where the flow direction changes from the axial direction to the radial direction, the streamwise velocity tends to become small near the casing (See Figure 13). In such situation, a streamwise vortex is easy to break down with adverse pressure gradient, because the velocity of vortex core flow is also small. Therefore, in the compressor C_B with the strong adverse pressure gradient in that area, that has led to the breakdown of the tip leakage vortex.

Effects of vortex breakdown Figure 12 shows the time-averaged Mach number distributions at 90% span at the near disturbance onset point. Comparing the sizes of the low velocity region between the compressors, it is obviously larger in the compressor C_B. The low velocity region is developing especially in the passage between the full blade suction surface and the splitter blade pressure surface, because the vortex breakdown occurs in the full blade tip leakage vortex. The vortex breakdown expands a vortex core radius drastically, which results in the significant expansion of the low velocity region in the compressor C_B. Therefore, the vortex breakdown leads to a large blockage effect by expanding the low velocity region.

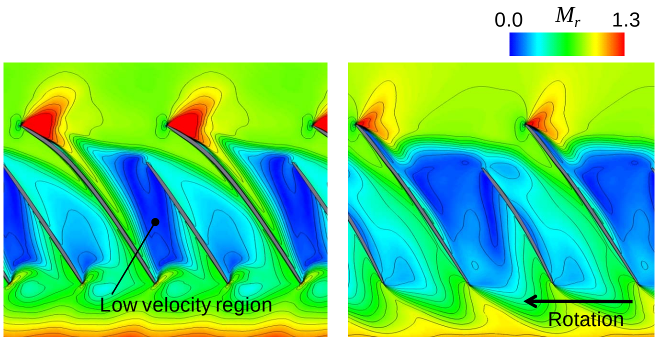

(a) compressor C_A (b) compressor C_B

Figure 12. Time-averaged Mach number distributions at 90% span at the near disturbance onset point (DES)

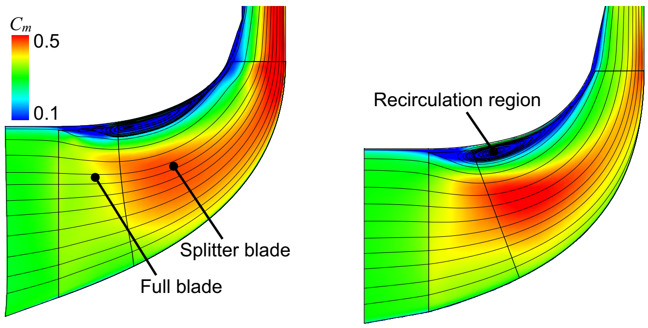

(a) compressor C_A (b) compressor C_B

Figure 13. Pitchwise-averaged flow fields on the meridional plane (DES)

Figure 13 shows streamlines of the pitchwise-averaged meridional flow. In both compressors, a recirculation region is formed on the casing wall from the impeller inlet to exit. This recirculation region, which results from the tip leakage flow, corresponds to the low velocity region. Therefore, the recirculation region is regarded as the blockage region. As expected, in the compressor C_B with the vortex breakdown, the blockage region is larger. It is seen that the blockage effect due to the vortex breakdown works in the spanwise direction rather than in the streamwise direction. Streamwise distributions of displacement thickness on the casing wall, which is calculated from the pitchwise-averaged meridional flow fields shown in Figure 13, is presented in Figure 14. The displacement thickness δ^* is defined as follows:

$$\delta^* = \int_0^\delta \left(1 - \frac{C_m}{C_m|_{y=\delta}}\right) dy \qquad (4)$$

where C_m is a local meridional velocity, and δ is a boundary layer thichness, which is defined as the distance from the casing wall where the meridional velocity has 99% of the maximum value. The displacement thickness is normalized by the inlet blade height of each compressor impeller. The abscissa is

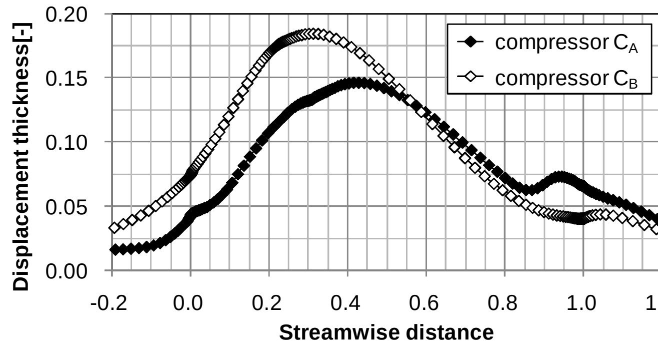

Figure 14. Streamwise distributions of displacement thickness on the casing wall (DES)

a streamwise distance along the casing wall. It has 0.0 at the leading-edge of the full blade, and 1.0 at the trailing-edge. After taking a peak inside the impeller, the displacement thickness decreases toward the impeller exit with progressive reduction in cross-sectional area of the passage and the recirculation region. It is clearly seen that the displacement thickness for the compressor C_B increases significantly due to the vortex breakdown. The discrepancy between two compressors is found on the upstream side from the peak and the blockage effect due to the vortex breakdown reaches the upstream of the impeller. In the compressor C_B, the displacement thickness is found to develop up to about 20% of the inlet blade height.

Distrubance Onset Flow Fields

Figure 15 shows the unsteady behaviors of Mach number distribution at 90% span and vortex core structures at the disturbance onset point. In the compressor C_A, the low velocity region is distributed nonaxisymmetrically. As will be shown later, since the passage covered with the low velocity region has large blockage effect, it brings about a leading-edge separation near the tip for the full blade on the opposite side to rotation direction, and generates a tornado-type separation vortex which makes the full blade stall. The tornado-type separation vortex gradually blocks the full blade passage with its growth, and then produces a new low velocity region. It follows that a new tornado-type separation vortex is induced on the next full blade and the blockage in the adjacent passage, which has generated the tornado-type separation vortex, decreases. Through repeating this series of flow events, the tornado-type separation vortex and the blockage region propagate in the impeller as a stall cell in the opposite direction to the rotation. It is found that the rotating stall is occurring in the compressor C_A.

On the other hand, in the compressor C_B, all the full blade passages are covered with the low velocity region due to the occurrence of the tip leakage vortex breakdown. In every full blade, there is no boundary layer separation and no tornado-type separation vortex. Therefore, the compressor C_B is not still in stall

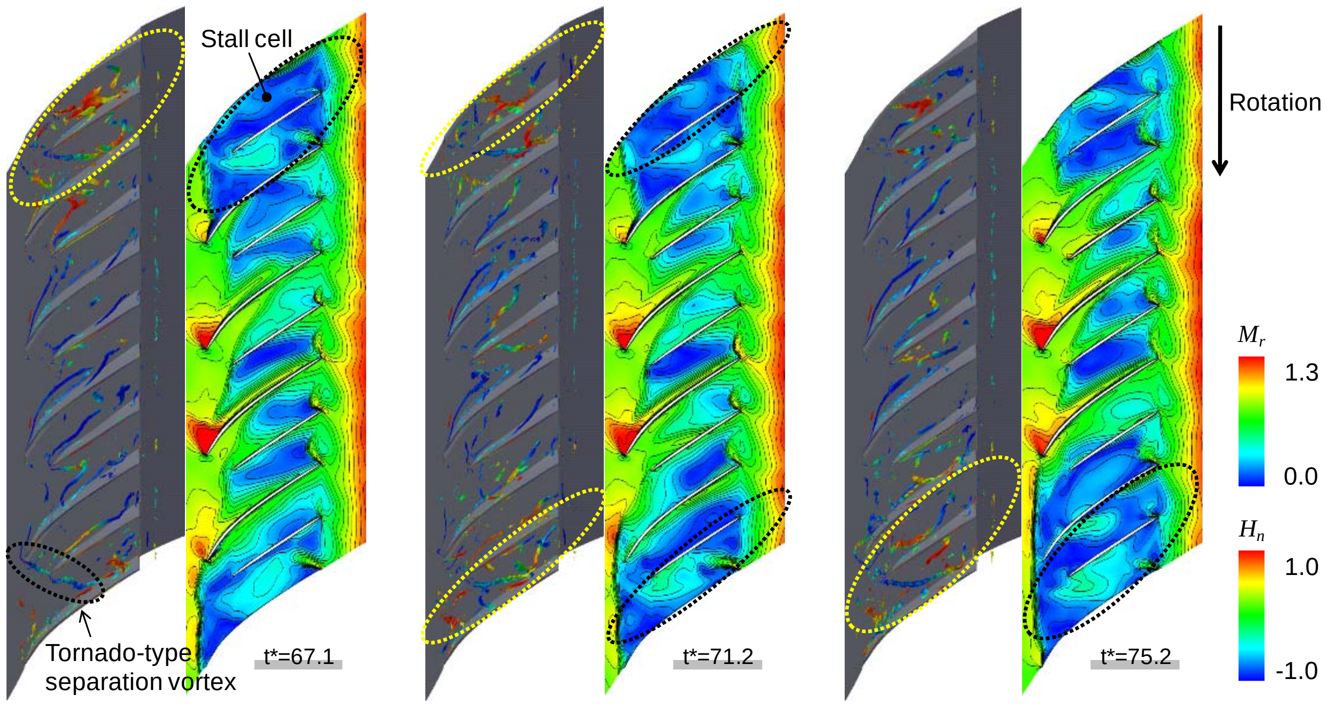

(a) compressor C_A (Q = 0.102 m^3/s)

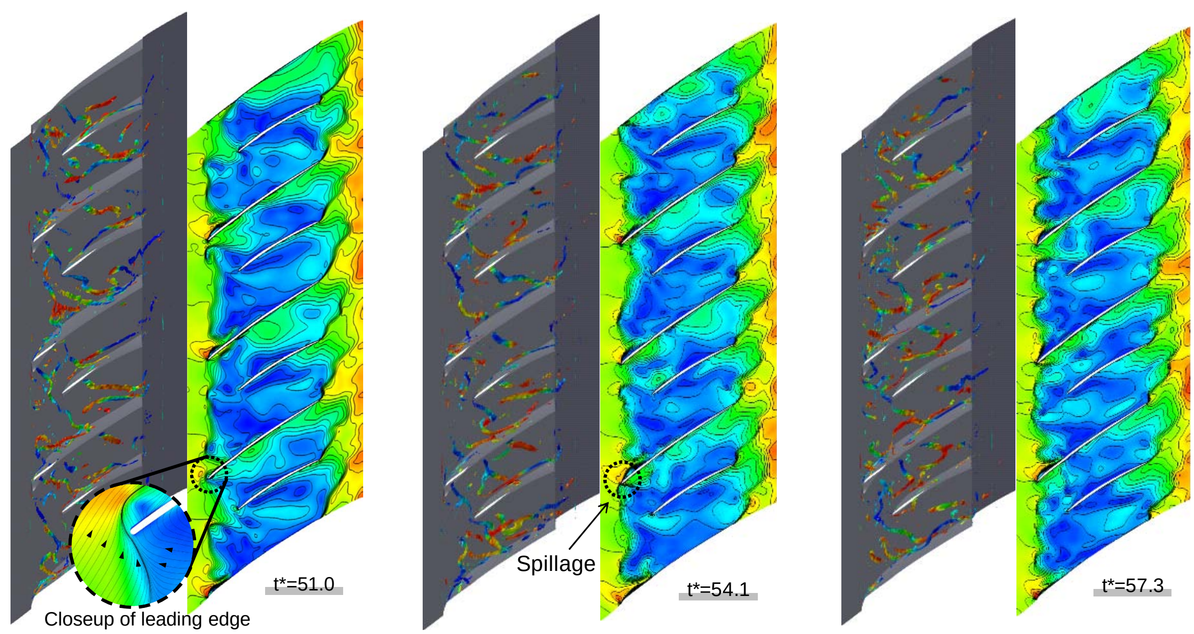

(b) compressor C_B (Q = 0.084 m^3/s)

Figure 15. Unsteady behaviors of Mach number distribution at 90% span (right) and vortex core structures colored with normalized helicity (left) at disturbance onset point (DES)

condition. Generally, in the rotating stall, the blockage region is assembled to form the stall cell and in the passages outside the stall cell the flow field returns to a sound condition with increasing flow rate. However, as discussed in the previous section, in the compressor C_B, the vortex breakdown has already happened before the disturbance onset, and generates the low velocity region with large blockage effect near the casing in all the passages. Since the flow field cannot return to a sound condition in every

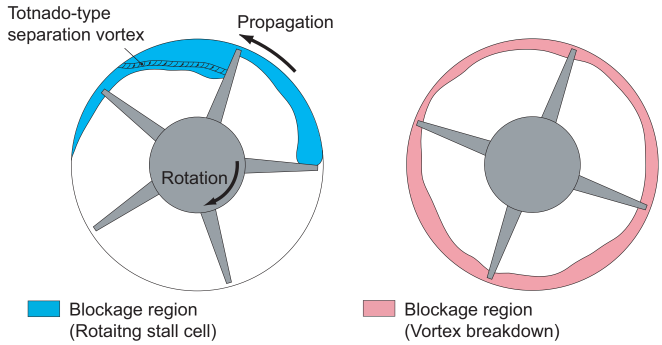

(a) compressor C_A (b) compressor C_B

Figure 16. Illustration of blockage regions inside impeller at disturbance onset point

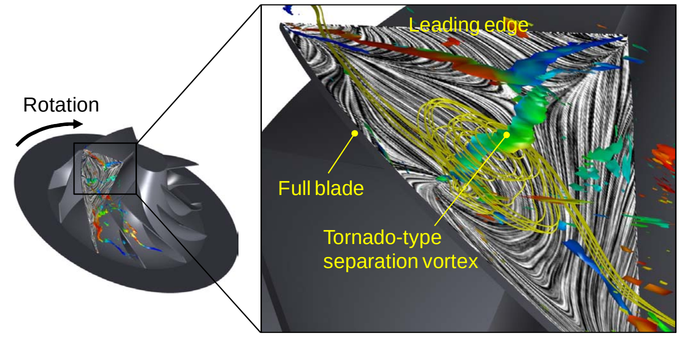

Figure 17. Instantaneous limiting streamline on the suction surface of the full blade and vortex core structures around the rotating stall cell in compressor C_A (DES)

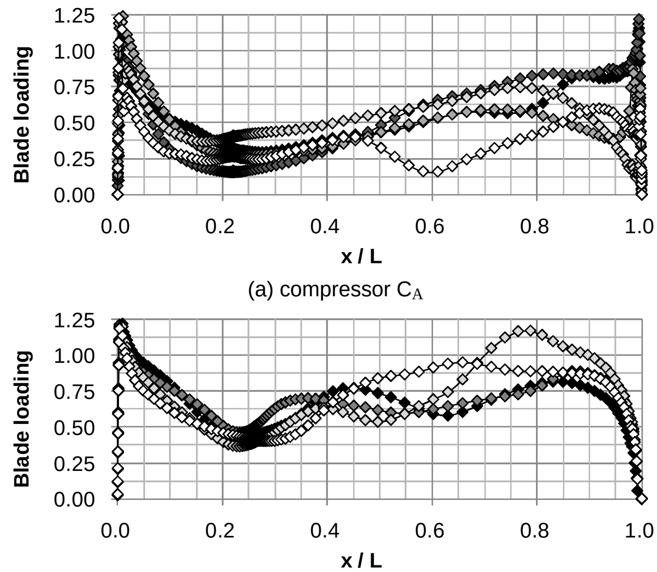

(a) compressor C_A

(b) compressor C_B

Figure 18. Instantaneous blade loading distributions of each full blade at mid span at disturbance onset point (DES)

passage, the blockage region is not able to form the stall cell. This is the reason why the rotating stall is not occurring in the compressor C_B.

It is found that a segment of the tip leakage vortex is being periodically shed due to an unsteady nature of the vortex breakdown, and interacting with the pressure surface of the adjacent full blade near the leading edge. The low velocity region extends to nearly the leading edge line of full blade, after the vortex breakdown is enhanced by decreased flow rate. Therefore, the vortex segments reach to the leading edge line and sometimes spills into the adjacent passage (See the bottom passage at t*=51.0 in the figure (b)). The vortex shedding leads to pressure fluctuation inside the impeller. On the caisng wall at the leading edge line, a pitchwise pressure distribution is generated by the presence of the shed vortex segments, and it rotates with the impeller. This is detected at the upstream of the impeller as the high frequency waves in the pressure traces shown in Figure 5. Moreover, the intermittent spillage of the vortex shedding is considered as a cause of the disturbance in the compressor C_B.

Figure 16 shows an illustration of the blockage regions inside the impeller at the disturbance onset point. As shown in the figure, the difference in off-design flow fields between the two compressors is restated as the difference in a pattern of the blockage region, namely whether the blockage region is locally accumulated in the impeller or not. However, there is a major difference in the cause of the blockage. In the compressor C_A, the blockage is generated by the tornado-type separation vortex resulting from the leading-edge separation, and rotates in the impeller as the stall cell. On the other hand, in the compressor C_B, the vortex breakdown generates the blockage. The leading-edge separation happens locally in the impeller, while the vortex breakdown happens concurrently in all the passages. Therefore, only the blockage in the compressor C_A can become the rotating stall cell. Figure 17 shows an instantaneous limiting streamline on the full blade suction surface and vortex core structures around the rotating stall cell in the compressor C_A. There is a focal point on the limiting streamline, from which a tornado-type separation vortex arises. The tornado-type separation vortex has resulted from the development of leading-edge separation near the tip and causes a significant decrease in the blade loading of full blade, which has resulted in the deterioration of the compressor performance at off-design condition (Refer to Figure 3). Figure 18 shows instantaneous blade loading distributions of each full blade at the mid span. In the compressor C_A, there is a blade with extremely reduced blade loading, on which the tornado-type separation vortex is occurring. In the case of the compressor C_B, there is not apparent decrease in the performance despite the occurrence of the vortex breakdown. The reason is that there is no decrease in the blade loading resulting from the leading-edge separation near the tip (See Figure 18). The leading-edge separation has not been able to occur near the tip, since the flow on

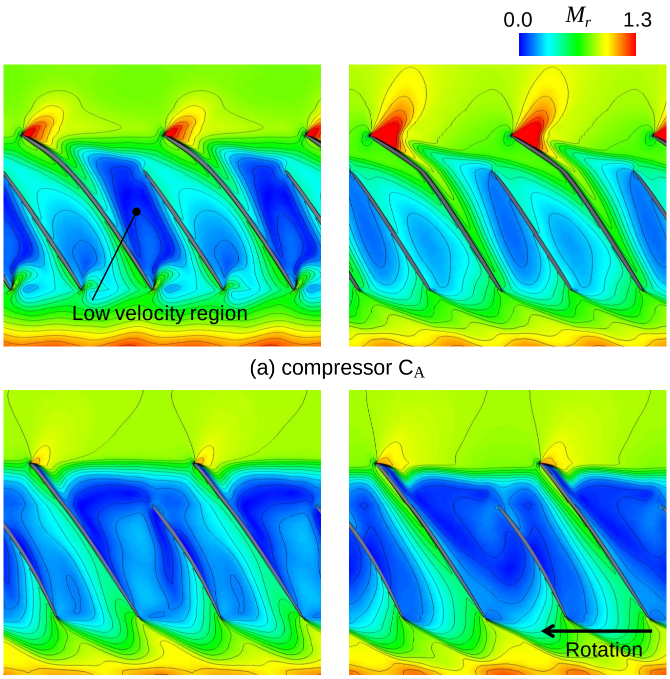

Figure 19. Mach number distributions at 90% span at disturbance onset point (left: time-averaged DES result, right: steady RANS result)

the tip side has been blocked by the breakdown region accompanied with reversed flow. It this way, the rotating stall consisting of the tornado-type separation vortex leads to performance deterioration and the vortex breakdown has an effect of suppressing the occurrence of the rotating stall. Therefore, the vortex breakdown plays an important role in achievement of high off-design performance.

Figure 19 shows the time-averaged Mach number distributions at 90% span at the disturbance onset point. The RANS results are also shown for comparison. In the compressor C_B, the low velocity region covers almost all over the full blade passage. On the other hand, in the compressor C_A, the low velocity region is relatively small in spite of the appearance of rotating stall and mostly remains in the pressure side passage of splitter blade without spilling into the suction side passage. The time-averaged DES result and the steady-state single passage RANS result are quite similar to each other for the compressor C_B, while they show a large quantitative difference for the compressor C_A. This difference in the compressor C_A corresponds to the discrepancy in the performance characteristics, which becomes larger with lower flow rate, shown in Figure 3. As mentioned above, the rotating stall occurs in the compressor C_A at this operating condition, and it is beyond the applicability limit of the steady-state single passage RANS calculation. Therefore, the difference is considered to be also attributed to this applicability limit of RANS calculation. In the compressor C_B, the vortex breakdown has occurred concurrently in all the passages without the occurrence of the rotating stall, and then every passage has a similar flow field. As a result, the time-averaged flow field from the DES is identical to the steady-state flow field from the single passage RANS calculation. This raises the issue in applying the steady-state single passage RANS calculation for prediction of off-design performance.

CONCLUSIONS

Two types of transonic centrifugal compressors with different aerodynamic characteristics were analyzed using the time-accurate DES (Detached-Eddy Simulation) to investigate the difference in the tip leakage flow fields. The results are summarized as follows:

1. In the compressor with higher performance at off-design condition, the vortex breakdown happened in the tip leakage vortex of the full blade. The vortex breakdown appeared in all the passages of the compressor impeller prior to the occurrence of disturbances.
2. The vortex breakdown greatly expanded the low velocity region, and led to a large blockage effect near the casing. Since every passage must constantly have had the large blockage region resulting from the vortex breakdown, the blockage could not be assembled to form stall cells. As a result, the vortex breakdown suppressed the rotating stall.
3. The tip leakage vortex periodically shed its segment due to an unsteady nature of the vortex breakdown. The vortex segment from the tip leakage vortex of full blade interacted with the pressure surface of the adjacent full blade near the leading edge, and sometimes spills into the adjacent passage with decreased flow rate, which resulted in the onset of the disturbance.
4. In the compressor with lower performance at off-design condition, the rotating stall started with the onset of the disturbance. In the stall cell, there was a focal-type separation on the suction surface of full blade, from which a tornado-type separation vortex was generated. The tornado-type separation vortex blocked the passage with its growth, and this blockage effect brought about a new tornado-type separation vortex on the adjacent blade to propagate the stall cell circumferentially in the compressor impeller.

ACKNOWLEDGMENT

The present research was partially supported by Japan Society for the Promotion of Science (JSPS), Grant-in-Aid for Scientific Research (B), KAKENHI 21360085, 2009.

REFERENCES

[1] Ibaraki, S., Furukawa, M., Iwakiri, K., and Takahashi, K., 2007. "Vortical flow structure and loss generation process

in a transonic centrifugal compressor impeller". ASME Paper GT2007-27791.

[2] Ibaraki, S., Sumida, K., and Suita, T., 2009. "Design and off-design flow fields of a transonic centrifugal compressor impeller". ASME Paper GT2009-59986.

[3] Hazby, H. R., and Xu, L., 2009. "Role of tip leakage in stall of a transonic centrifugal impeller". ASME Paper GT2009-59372.

[4] Furukawa, M., Inoue, M., Saiki, K., and Yamada, K., 1999. "The role of tip leakage vortex breakdown in compressor rotor aerodynamics". *ASME J. Turbomachinery,* ***121***(3), pp. 469–480.

[5] Furukawa, M., Saiki, K., Yamada, K., and Inoue, M., 2000. "Unsteady flow behavior due to breakdown of tip leakage vortex in an axial compressor rotor at near-stall condition". ASME. Paper No. 2000-GT-666.

[6] Schlechtriem, S., and Lotzerich, M., 1997. "Breakdown of tip leakage vortices in compressors at flow conditions close to stall". ASME Paper No. 97-GT-41.

[7] Yamada, K., Furukawa, M., Nakano, T., Inoue, M., and Funazaki, K., 2004. "Unsteady three-dimensional flow phenomena due to breakdown of tip leakage vortex in a transonic axial compressor rotor". ASME Paper GT2004-53745.

[8] Yamada, K., Funazaki, K., and Furukawa, M., 2007. "The behavior of tip clearance flow at near-stall condition in a transonic axial compressor rotor". ASME Paper GT2007-27725.

[9] Eckardt, D., 1976. "Detailed flow investigations within a high speed centrifugal compressor impeller". *ASME J. Fluids Engineering,* ***98***, pp. 390–402.

[10] Krain, H., 1988. "Swirling impeller flow". *ASME J. Turbomachinery,* ***110***, pp. 122–128.

[11] Hah, C., and Krain, H., 1990. "Secondary flows and vortex motion in a high-efficiency backswept impeller at design and off-design condition". *ASME J. Turbomachinery,* ***112***, pp. 7–13.

[12] Senoo, Y., and Ishida, M., 1987. "Deterioration of compressor performance due to tip clearance of centrifugal impellers". *ASME J. Turbomachinery,* ***109***(1), pp. 55–61.

[13] Schleer, M., Song, S. J., and Abhari, R. S., 2006. "Clearance effects on the onset of instability in a centrifugal compressor". ASME Paper GT2006-90084.

[14] Iwakiri, K., Furukawa, M., Ibaraki, S., and Tomita, I., 2009. "Unsteady and three-dimensional flow phenomena in a transonic centrifugal compressor impeller at rotating stall". ASME Paper GT2009-59516.

[15] Wilcox, D. C., 1994. "Simulation of transition with a two-equation turbulence model". *AIAA Journal,* ***32***(2), pp. 247–255.

[16] Strelets, M., 2001. "Detached eddy simulation of massively separated flows". In Proceedings of 29th Fluid Dynamic Conference, AIAA. Paper 2001-0879.

[17] Yamada, K., Tamagawa, Y., Fukushima, H., Furukawa, M., Ibaraki, S., and Iwakiri, K., 2010. "Comparative study on tip clearance flow fields in two types of transonic centrifugal compressor impeller with splitter blades". ASME Paper GT2010-23345.